

Micromachined cantilevers-on-membrane topology for broadband vibration energy harvesting

This content has been downloaded from IOPscience. Please scroll down to see the full text.

2016 J. Micromech. Microeng. 26 124007

(<http://iopscience.iop.org/0960-1317/26/12/124007>)

View [the table of contents for this issue](#), or go to the [journal homepage](#) for more

Download details:

IP Address: 131.111.184.102

This content was downloaded on 27/01/2017 at 12:47

Please note that [terms and conditions apply](#).

You may also be interested in:

[Comparison of Five Topologies of Cantilever-based MEMS Piezoelectric Vibration Energy Harvesters](#)

Y Jia and A A Seshia

[Parametric resonance for vibration energy harvesting with design techniques to passively reduce the initiation threshold amplitude](#)

Yu Jia, Jize Yan, Kenichi Soga et al.

[Parametrically excited MEMS vibration energy harvesters with design approaches to overcome the initiation threshold amplitude](#)

Yu Jia, Jize Yan, Kenichi Soga et al.

[Modeling and characterization of MEMS-based PHDs](#)

T M Kamel, R Elfrink, M Renaud et al.

[Fabrication and analysis of high-performance piezoelectric MEMS generators](#)

Gang Tang, Jing-quan Liu, Bin Yang et al.

[A vibration energy harvesting device with bidirectional resonance frequency tunability](#)

Vinod R Challa, M G Prasad, Yong Shi et al.

[White Noise Responsiveness of an AIN Piezoelectric MEMS Cantilever Vibration Energy Harvester](#)

Y Jia and A A Seshia

[A nonlinear stretching based electromagnetic energy harvester on FR4 for wideband operation](#)

Dhiman Mallick, Andreas Amann and Saibal Roy

[A micromachined low-frequency piezoelectric harvester for vibration and wind energy scavenging](#)

Xuefeng He, Zhengguo Shang, Yaoqing Cheng et al.

Micromachined cantilevers-on-membrane topology for broadband vibration energy harvesting

Yu Jia^{1,2}, Sijun Du¹ and Ashwin A Seshia¹

¹ Department of Engineering, University of Cambridge, Trumpington Street, Cambridge CB2 1PZ, UK

² Department of Mechanical Engineering, University of Chester, Thornton Science Park, Chester CH2 4NU, UK

E-mail: yu.jia.gb@ieee.org, sd672@cam.ac.uk and aas41@cam.ac.uk

Received 7 March 2016, revised 17 June 2016

Accepted for publication 26 July 2016

Published 17 October 2016



Abstract

The overwhelming majority of microelectromechanical piezoelectric vibration energy harvesting topologies have been based on cantilevers, doubly-clamped beams or basic membranes. While these conventional designs offer simplicity, their broadband responses have been limited thus far. This paper investigates the feasibility of a new integrated cantilevers-on-membrane design that explores the optimisation of piezoelectric strain distribution and improvement of the broadband power output. While a classic membrane has the potential to offer a broader resonant peak than its cantilever counterpart, the inclusion of a centred proof mass compromises its otherwise high strain energy regions. The proposed topology addresses this issue by relocating the proof mass onto subsidiary cantilevers and combines the merits of both the membrane and the cantilever designs. Numerical simulations, constructed using fitted values based on finite element models, were used to investigate the broadband response of the proposed design in contrast to a classic plain membrane. Experimentally, when subjected to a band-limited white noise excitation, the new cantilevers-on-membrane harvester exhibited nearly two fold power output enhancement when compared to a classic plain membrane harvester of a comparable size.

Keywords: piezoelectric, vibration energy harvesting, membrane, broadband

 Online supplementary data available from stacks.iop.org/JMM/26/124007/mmedia

(Some figures may appear in colour only in the online journal)

1. Introduction

In recent years, there has been a growing convergence between microelectromechanical systems (MEMS) and vibration energy harvesting (VEH) technologies [1], in an attempt to drive towards chip-level integrated implementations of MEMS VEH-powered IC platforms for sensors and wireless systems. Such development and integration hold the promise to eventually achieve maintenance-free distributed smart microsystems

that have the ability to replenish their own electrical energy by tapping into ambient sources, such as kinetic vibration.

Amongst the different types of miniaturised mechanical-to-electrical transduction mechanisms, electromagnetism typically does not scale well at dimensions typical of MEMS devices [2], while electrostatic generators generally demonstrate poor power densities [3]. While there has been a growing trend of adopting electret transducers [4, 5] and a recent emergence of triboelectric generators [6], piezoelectric films remain the most popular choice for MEMS VEH to date [7–9]. This is due to their power density scalability and the relative compatibility of piezoelectric materials such as aluminium nitride (AlN) and zinc oxide (ZnO) with MEMS



Original content from this work may be used under the terms of the [Creative Commons Attribution 3.0 licence](https://creativecommons.org/licenses/by/3.0/). Any further distribution of this work must maintain attribution to the author(s) and the title of the work, journal citation and DOI.

fabrication processes, in comparison with electromagnetic generators [3]. Furthermore, traditionally bulk piezoelectric materials such as lead zirconate titanate (PZT) have been integrated with MEMS fabrication processes [10, 11].

However, the superiority of the traditionally high charge constant bulk materials such as PZT over more readily MEMS compatible material such as AlN has yet to be established, and AlN has been reported to be as good of a MEMS-scale piezoelectric material compared to PZT [7]. Taking into account a range of other properties such as dielectric constant and elastic modulus, PZT only has a marginal theoretical power output advantage over AlN [8]. There has also been research to develop lead-free alternatives to PZT such as sodium potassium niobate (KNN) [12, 13], which also have relatively high charge constants.

In terms of topologies, cantilever-based designs are by far the most employed structure [7, 8, 14]. This is primarily due to their simplicity, high responsiveness and the ability to house a proof mass near the free end without compromising the high strain energy regions of the active piezoelectric transducer near the anchor [15, 16]. Furthermore, as a cantilever only has one strain region when operating at the fundamental mode, electrode configuration is also typically simple.

Aktakka *et al* [11] investigated the incorporation of a tungsten mass into a MEMS cantilever in order to realise a more dense proof mass for enhancing the power density. The inclusion of a tungsten mass [11] compared favourably against a similar device with a silicon mass [17] in terms of normalised power density: $10.1 \text{ mW cm}^{-3} \text{ g}^{-2}$ in contrast to $5 \text{ mW cm}^{-3} \text{ g}^{-2}$. However, another study that employed cantilevers with silicon mass, but also explored the optimisation of the mass to length ratio, demonstrated an even better result: $15.0 \text{ mW cm}^{-3} \text{ g}^{-2}$ [14]. Therefore, careful optimisation of a range of parameters such as maximising mass density, optimising mass to length ratio, piezoelectric layer to substrate layer thickness ratio and choice of a specific topological design [16] are all critical to engineer a MEMS cantilever-based harvester.

Meanwhile, a few studies in the field [3, 9] have also investigated other membrane based topologies. Membranes are inherently more nonlinear and have the potential to experience higher strain energy for the same level of displacement. However, notable power or bandwidth enhancements from membrane designs have yet to be experimentally demonstrated [18].

One of the main drawbacks of the membrane topology, in comparison to a cantilever-based design, is the inevitable strain neutralisation of active piezoelectric transduction regions with the addition of an effective proof mass. Figure 1 shows the FEA simulation of a circular disk membrane, without any proof mass. It can be seen that, under mechanical loading, the membrane experiences maximum strain around the centre. Therefore, the piezoelectric films that cover the centre regions can harvest relatively more strain energy. On the other hand, figure 2 illustrates a scenario where a significant area of the otherwise high strain energy region of a circular disk membrane is sacrificed to house a centred proof mass, in order to improve the responsiveness of the resonator.

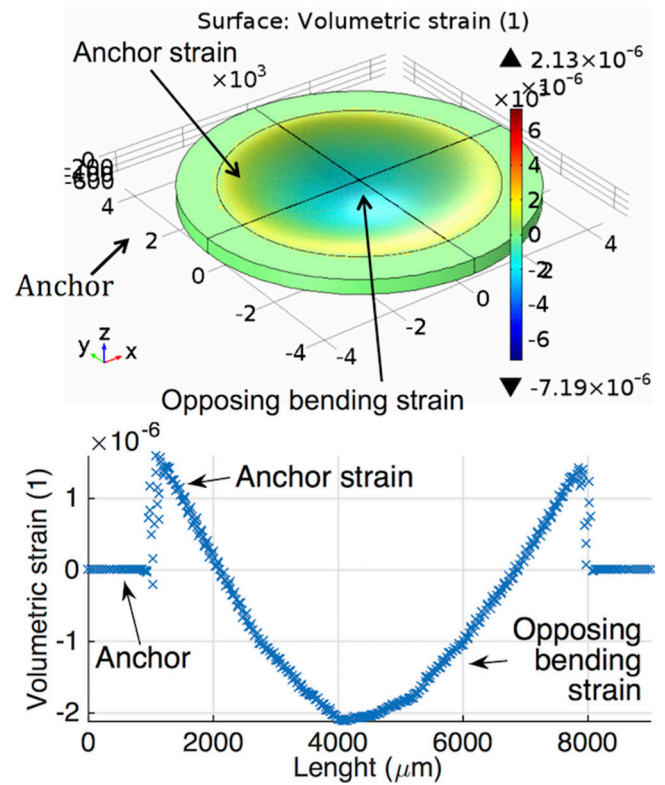


Figure 1. COMSOL model of a plain classic circular disk membrane (7 mm diameter) and the radial strain distribution when subjected to an acceleration loading of 100 g on the proof mass.

Since a given piezoelectric harvester relies on strain-induced charge generation across its active transduction area, strain optimisation is of paramount importance for power optimisation. Furthermore, the additional clamping conditions in a membrane structure yield lower compliance; thus, the membrane requires a higher excitation to manifest the same level of mechanical strain when compared to a cantilever beam.

2. Design

A cantilevers-on-membrane topology [19] is proposed in figures 3 and 4, in an attempt to improve both the responsivity towards broadband excitation and achieve better strain optimisation for a membrane-based design. Instead of placing a single proof mass at the membrane centre, the masses are distributed on subsidiary cantilevers that extend outwards from the centre.

Although regions of the membrane are still sacrificed to accommodate the mass, the constant high strain regions of the membrane core are freed up for the piezoelectric transducer (figure 5). Additionally, the subsidiary cantilevers themselves comprises high strain regions (see figure 4). Similar to a classic membrane structure, the membrane portion of the new design is composed of two opposing strain regions: the anchor strains near the clamped end and the bending strain near the centre. The bending strain of cantilevers align with that of the membrane core, thereby simplifying electrode design.

Table 1 summarises a simulated and calculated example where the proof mass of the device is subjected to 100 g of

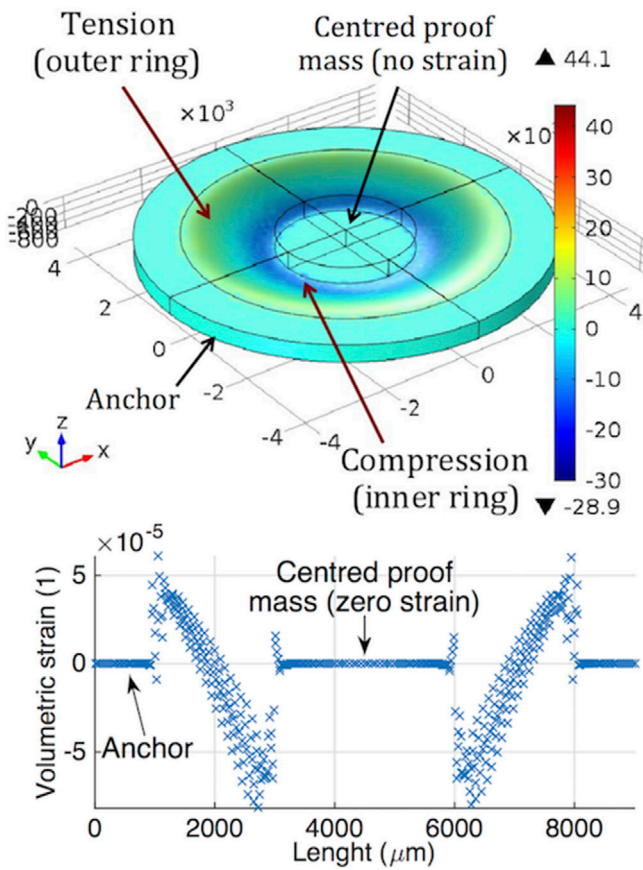


Figure 2. COMSOL model of a classic circular disk membrane (7 mm diameter) with a centred circular suspended proof mass (3 mm diameter) and the radial strain distribution when subjected to an acceleration loading of 100 g on the proof mass.

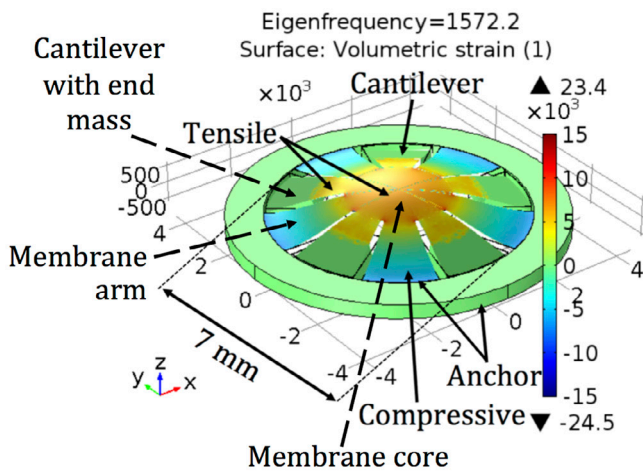


Figure 3. COMSOL model of the integrated cantilever-membrane design with the proof mass distributed on subsidiary cantilevers.

acceleration loading on the proof mass. Note that this is not the base acceleration but the shuttle acceleration. This level of acceleration loading was chosen in order to simulate the representative shuttle acceleration experienced by the oscillator at resonance. In the simulation, 0.5 μm thick aluminium nitride (AlN) is assumed as the piezoelectric layer. It can be seen that

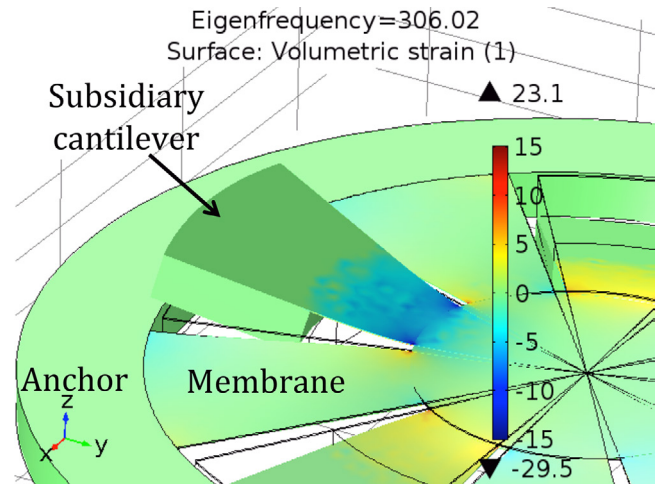


Figure 4. Zoomed-in view of the proposed topology showing a subsidiary cantilever attached to the membrane core. The current prototype has five subsidiary cantilevers, segregated by an arm of the membrane between each cantilever.

the design complexity of the new membrane topology resulted in smaller total active piezoelectric area. However, as a result of higher compliance of the etched membrane structure as well as the larger effective proof mass, the average induced strain is several folds higher.

The theoretical maximum power extractable from the simulated strain response was calculated by computing the average electric charge generated by equation (1) and the power extractable across an ideal impedance given by equation (2) [20].

$$q = d_{31}\epsilon_{av}Ea_{pz} \quad (1)$$

where q is the short circuit charge generated, d_{31} is the piezoelectric charge constant in the 31 mode, ϵ_{av} is the average induced strain, E is the elastic modulus and a_{pz} is the active piezoelectric area.

$$P = \frac{R_s^2 + X_s^2}{2(R_L + R_s)}(\omega q)^2 \quad (2)$$

where P is the maximum power extractable across a matched resistive load, ω is the angular frequency, R_L is the matched resistive load, R_s is the internal resistance and X_s is the internal reactance.

Table 1 compares a scenario where given the same design area, the new membrane has the potential to attain significantly higher peak power. Most noticeably, the new design provides additional strain energy from the membrane core, which otherwise would have been sacrificed to housing a centred mass. Furthermore, the additional subsidiary cantilevers also contribute high strain energy regions when operated into resonance at different frequencies. However, this theoretical value is only achievable if all the various active piezoelectric regions are optimally matched in impedance. In practice, due to the complexity of the structure, it is difficult to simultaneously extract maximum energy from both the membrane and the subsidiary cantilevers.

Table 1. Comparison of classic disk membrane and cantilevers-on-membrane designs for the same given design area (3.5 mm active radius).

Parameter	Classic disk membrane		Cantilevers-on-membrane	
	Area (m ²)	av. strain (1)	Area (m ²)	av. strain (1)
<i>Strains:</i>				
Membrane anchor	1.88×10^{-5}	2.02×10^{-5}	7.85×10^{-6}	1.03×10^{-4}
Membrane bending	1.26×10^{-5}	4.07×10^{-5}	5.23×10^{-6}	1.86×10^{-4}
Membrane core bending	n/a	n/a	7.07×10^{-6}	1.29×10^{-04}
Cantilever bending	n/a	n/a	3.98×10^{-6}	2.62×10^{-4}
Proof mass (kg)	6.56×10^{-6}		8.45×10^{-6}	
Natural frequency 01 mode (Hz)	1478		1572	
Area \times av. strain (m ²)	8.91×10^{-10}		3.73-9	
Charge generated (C)	5.88×10^{-10}		2.46×10^{-9}	
Theoretical peak power (W)	6.41×10^{-7}		1.56×10^{-5}	

Note: Accumulated strain across the active piezoelectric area when subjected to an acceleration loading of 100 g, corresponding to maximum theoretically achievable power amplitude assuming optimal impedance matching for all constituent piezoelectric regions. Av. strain represents average strain across a particular active piezoelectric region.

3. Modelling

3.1. Model

A numerical model was constructed partially through analytical derivation and partially through regression fit of an FEA model. See the supplementary material for details (stacks.iop.org/JMM/26/124007/mmedia).

3.1.1. Disk membrane. For a thin circular membrane, the deflection curve takes the form of a parabola and can be described by equation (3) [21]:

$$\delta(r) = \delta_{\max} \left(1 - \frac{r^2}{R^2}\right) \quad (3)$$

where $\delta(r)$ is the deflection along the radial axis r , δ_{\max} is the maximum deflection amplitude and R is the radius of the membrane.

For a resonator subjected to a direct dynamic forcing $F(t)$, the dynamic response is approximated by equation (4):

$$\frac{F(t)}{m} = A\omega^2 \cos(\omega t) = \ddot{x} + 2\zeta\omega_n\dot{x} + \omega_n^2x + \frac{\mu}{m}x^3 \quad (4)$$

where x is the response displacement, ζ is the damping ratio, m is the effective mass, μ is the Duffing coefficient, ω_n is the natural frequency, A is the excitation displacement amplitude, ω is the excitation frequency and t is the time domain.

The resultant force F_r experienced by the effective mass, with phase angle ϕ , can thus be represented by equation (5):

$$F_r(t) = m\ddot{x}(t) = mx\omega^2 \cos(\omega t + \phi). \quad (5)$$

For a disk membrane with a centred proof mass that experiences resultant force amplitude F_r , the governing equation is presented in equation (6) [21]:

$$F_r = \pi h \delta_{\max} \left(\frac{c_1 h^2 E}{R^2(1-\nu^2)} + 4\sigma_0 + \frac{c_2 \delta_{\max}^2 E}{R^2} \right) \quad (6)$$

where

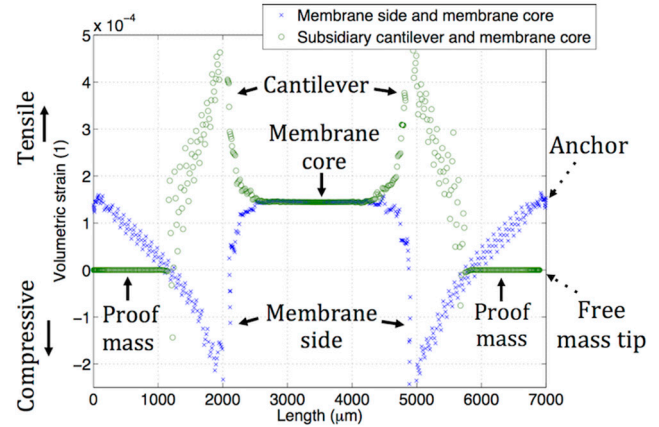


Figure 5. Strain distribution of the integrated cantilever membrane design for 100 g acceleration loading. The centre of the membrane experiences notable strain.

$$c_1 = \frac{16}{3 \left(1 - \frac{R_m^4}{R^4} - \frac{4R_m^2}{R^2} \ln \frac{R}{R_m}\right)} \quad (7)$$

$$c_2 = \frac{(7-\nu) \frac{(1 + \frac{R_m^2}{R^2} + \frac{R_m^4}{R^4})}{3} + (3-\nu)^2 \frac{R_m^2}{(1+\nu) R^2}}{(1-\nu) \left(1 - \frac{R_m^4}{R^4}\right) \left(1 - \frac{R_m^2}{R^2}\right)} \quad (8)$$

where, σ_0 is the residual stress, E is the elastic modulus, ν is the Poisson's ratio, R is the radius of the membrane and R_m is the radius of the mass.

Equation (6) can then be simplified to equation (9):

$$d_2 \delta_{\max}^3 + d_1 \delta_{\max} - m\ddot{x}(t) = 0 \quad (9)$$

where,

$$d_1 = \frac{c_1 h^3 E \pi}{R^2(1-\nu^2)} + 4\sigma_0 \pi h \quad (10)$$

$$d_2 = \frac{c_2 E \pi h}{R^2}. \quad (11)$$

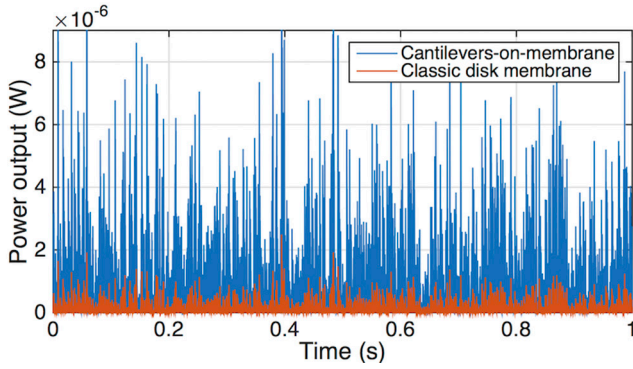


Figure 6. Simulated time-domain response of the classic and the proposed topologies when subjected to $0.13 \text{ g}^2 \text{ Hz}^{-1}$ of band-limited white noise (10 Hz to 2 kHz).

The only non-complex root of equation (9) is given by equation (12).

$$\delta_{\max} = \left(\frac{F_r}{2d_2} + \left(\frac{d_1^3}{27d_2^3} + \frac{F_r^2}{4d_2^2} \right)^{\frac{1}{2}} \right)^{\frac{1}{3}} - \frac{d_1}{3d_2 \left(\frac{F_r}{2d_2} + \left(\frac{d_1^3}{27d_2^3} + \frac{F_r^2}{4d_2^2} \right)^{\frac{1}{2}} \right)^{\frac{1}{3}}} \quad (12)$$

3.1.2. COMSOL fit. The deflection curve along the radial axis of the disk membrane with the centred mass was exported from a COMSOL model. This was subsequently used, alongside equation (12), to enable regression fit for the deflection curve model up to a 6th order polynomial equation. This enabled the construction of COMSOL fitted deflection, moment and stress equations as functions of the radial axis.

$$p_6 r^6 - p_5 r^5 + p_4 r^4 - p_3 r^3 + p_2 r^2 - p_1 r + p_0 = \delta(r) \quad (13)$$

$$M = -EI \frac{d^2 \delta(r)}{dr^2} \quad (14)$$

$$\sigma(r) = \frac{Mz}{I} = -Ez \frac{d^2 \delta(r)}{dr^2} \quad (15)$$

$$\sigma(r) = -Ez(q_4 x^4 - q_3 x^3 + q_1 x^2 - q_1 x + q_0) \quad (16)$$

where, p_i and q_i are fitted constant coefficients for the functions, M is the bending moment, z is the distance from the neutral axis to the surface, I is the area moment of inertia and $\sigma(r)$ is the induced stress along the radius axis r .

A polynomial fit was carried out with Q assumed to be 30. The fitted relationship between power amplitude P and maximum displacement for a membrane with $R = 3500 \mu\text{m}$, $R_m = 1500 \mu\text{m}$, silicon thickness of $10 \mu\text{m}$ and AlN thickness of $0.5 \mu\text{m}$ is given by equation (17):

$$P = u_2 \delta_{\max}^2 + u_1 \delta_{\max} - u_0 \quad (17)$$

where, for the given parameters here, $u_2 = 9.22 \times 10^4$, $u_1 = 2.25 \times 10^{-4}$ and $u_0 = 5.17 \times 10^{-9}$.

3.1.3. Cantilevers-on-membrane. The membrane section of the new design follows a similar deflection response derived in equation (13), albeit with changes to the coefficients due to

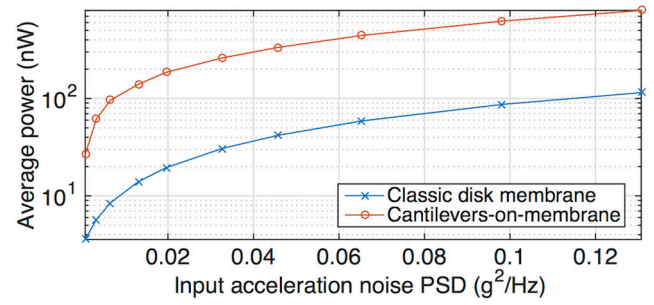


Figure 7. Simulated power response of the classic and the proposed topologies when subjected to band-limited white noise (10 Hz to 2 kHz).

varying effective mass, natural frequency and active area. The centre core region of the design that now consists of a strained active disk is assumed to have been subjected to a constant stress σ_{\max} across the given area (as illustrated in figure 5).

The cantilevers are modelled as coupled resonators subjected to the vibrational motion $x(t)$. The natural frequency ω_0 of the subsidiary cantilevers were modelled based on equation (18) [22]:

$$\omega_0^2 = \beta \frac{EI}{ml^3} \quad (18)$$

where, β is a fitted parameter based on the COMSOL model; and $\beta = 1.876$ for the fundamental mode of a clamped cantilever beam [22]. However, the subsidiary cantilevers are not strongly clamped to an anchor in this instance.

The response of the cantilevers are then modelled by equation (19):

$$\ddot{y}_i + 2\zeta_i \omega_{0i} \dot{y}_i + \omega_{0i}^2 y_i = x \omega^2 \cos(\omega t + \phi) \quad (19)$$

where y_i is the maximum displacement for the i th subsidiary cantilever.

Through the same process of regression fit towards the COMSOL model, a fitted relationship between power and displacement was derived (equation (20)) for the subsidiary cantilevers with the specific set of parameters chosen here (see the supplementary material for details):

$$P = v_2 y^2 - v_1 y - v_0 \quad (20)$$

where, for the given parameters here, $v_2 = 2.31$, $v_1 = 2.25 \times 10^{-6}$ and $v_0 = 4.77 \times 10^{-11}$.

3.2. Simulation

The numerical model thus constructed was used to simulate the response of a classic disk membrane device and a cantilevers-on-membrane device. Figure 6 shows the time domain power response of the devices when subjected to $0.13 \text{ g}^2 \text{ Hz}^{-1}$ of band-limited white noise (10 Hz to 2 kHz). Approximately sevenfold enhancement was seen in terms of the raw average power for the new proposed device design.

The response contrast between the two device designs towards broadband excitation is further highlighted in figure 7. The enhancement in power output came from both high power response from the membrane resonator of the new design, as

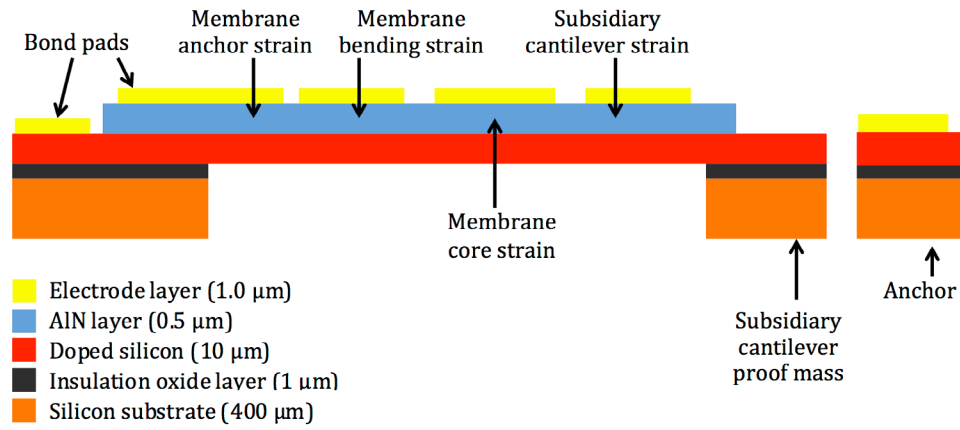


Figure 8. Stack of materials used in the MEMS fabrication process. This particular cross-sectional view illustrates part of the membrane on the left hand side and a subsidiary cantilever on the right hand side.

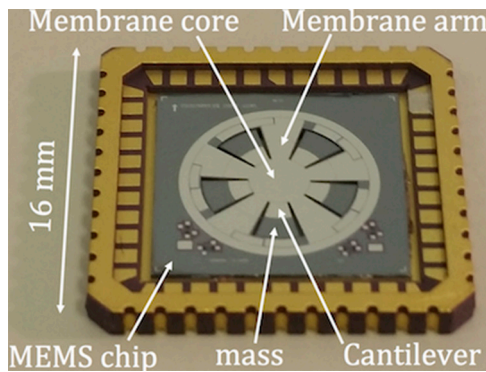


Figure 9. Photograph of the MEMS chip (12 mm by 12 mm) on a leadless chip carrier.

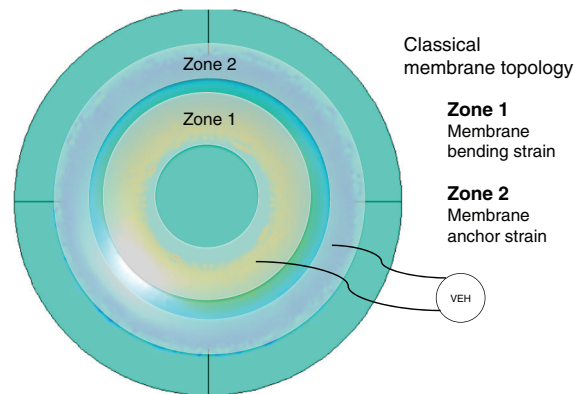


Figure 11. Electrode routing of the classic disk membrane device.

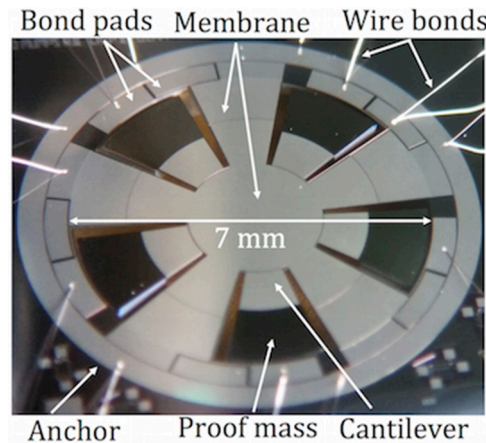


Figure 10. Cantilevers-on-membrane (7 mm active diameter) close-up view.

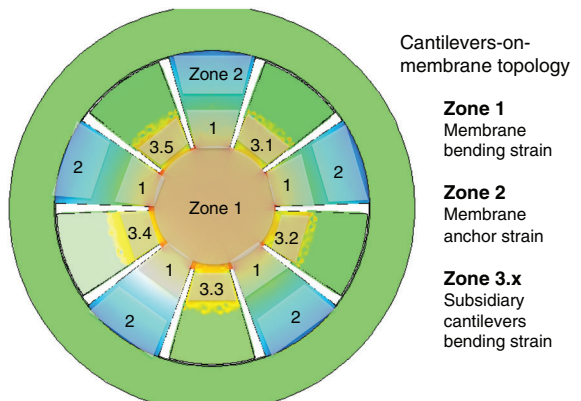


Figure 12. Electrode routing of the cantilevers-on-membrane device.

well as the additional responsiveness of the subsidiary cantilevers at lower frequencies.

4. Experimental

4.1. Fabrication and device

The harvester devices were micro-fabricated using a 0.5 μm aluminium nitride (AlN) on 10 μm doped silicon-on-insulator process, as outlined in figure 8. The piezoelectric and silicon

device layers sit on top of a 400 μm thick silicon substrate. Certain regions of the un-etched substrate layer were utilised as suspended proof masses.

Figure 9 shows a MEMS chip mechanically attached to a leadless chip carrier (LCC) using an epoxy adhesive. The bottom of the LCC was hollowed out by laser micromachining, in order to accommodate unrestricted shuttle travel of the proof masses and to minimise nonlinear film-squeeze damping within the package. Figure 10 presents a zoomed in view of the device, where it can be seen that the top metallisation does not cover proof masses.

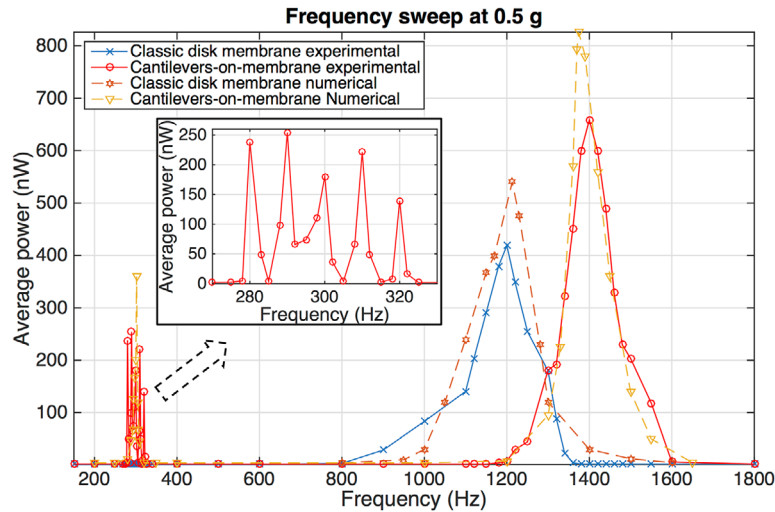


Figure 13. Frequency domain power response.

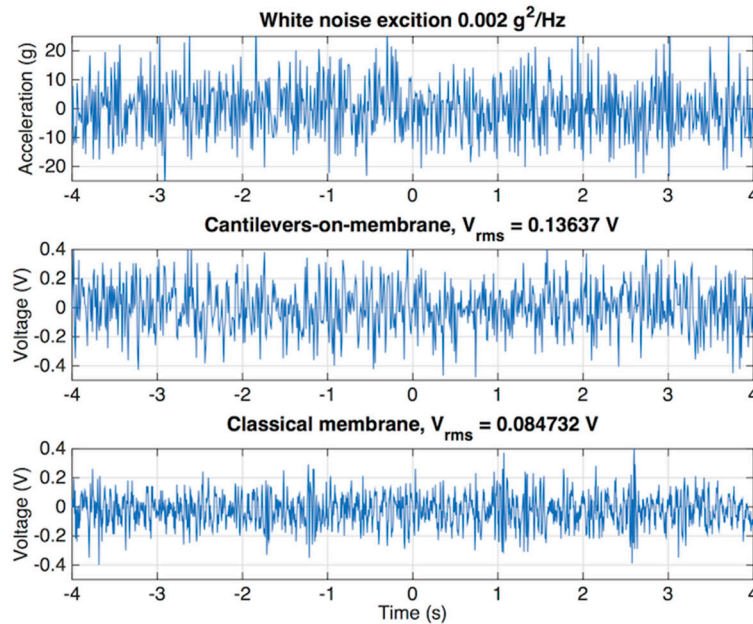


Figure 14. Time domain voltage response of the devices when subjected to band-limited white noise (10 Hz to 2 kHz).

The membrane total diameter is 7 mm and the core diameter is 3 mm, while the end mass on each subsidiary cantilever takes up approximately 60% of the cantilever length. The masses of each cantilever were intentionally subjected to small parameter variations in order to result in varying resonant frequencies. A classic disk membrane device (7 mm membrane diameter and 3 mm centred mass diameter) was also fabricated using the same process for comparison.

4.2. Electrode segmentation

Due to varying strain polarity across a membrane-based device, electrode regions were segmented into distinct zones. A classic disk membrane only possesses two zones as shown in figure 11. For the fundamental membrane mode, when zone 1 experiences compressive strain, zone 2 would be subjected to tension; and vice versa. Since the two opposing polarities

are from the same physical resonator, there is no frequency or phase mismatch. Therefore, by routing out zones 1 and 2, an AC source can be established. This also implies that the minimum number of wire bonds required to route out the piezoelectric transducer for a plain membrane is the same as that required for a plain cantilever harvester.

On the other hand, the cantilevers-on-membrane design requires a more complicated electrode segmentation configuration in order to maximise the power output. Generally, the same zone 1 and 2 membrane AC source can still be achieved as shown in figure 12 for the fundamental membrane mode. Zone 2 electrodes are located at various positions along the outer perimeter of the same global membrane resonator; they all harvest anchor strain in the same polarity and phase. Therefore, electrodes located on zone 2 are electrically linked together on the anchor of the die. In addition to the membrane electrodes, the bending strain areas of each of the subsidiary

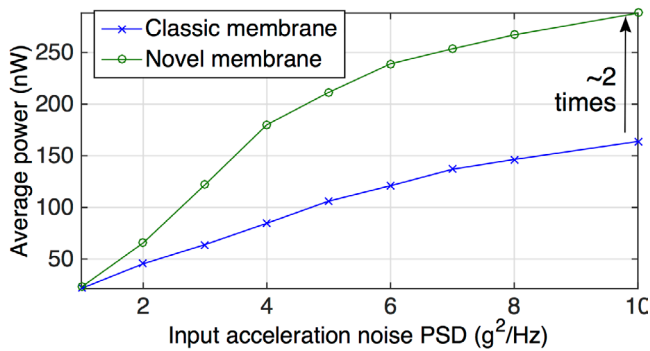


Figure 15. Measured average power for a classic membrane device and a new cantilevers-on-membrane device, subjected to band-limited white noise (10 Hz to 2kHz).

cantilevers are covered with zone 3.x electrodes, where x denotes the cantilever number.

As each of the subsidiary cantilevers are only weakly coupled from one another at their respective anchor, zone 3.x electrodes should ideally be routed out separately due to the frequency and phase mismatch between each of the cantilever oscillators. Even when designed to be identical, fabrication tolerances will almost always result in a slight frequency mismatch between each of the cantilevers. If all of the cantilevers are connected together as a single electrical region, then there would be time periods when their output amalgamate, while there would also be time periods when their individual output would cancel each other out.

While individual electrode zones were thus segmented during layout design and fabrication, all transduction regions with the same strain polarity were connected together (off chip) for experimental simplicity. This however came at the cost of sub-optimal impedance matching and power extraction from the harvester, as well as the phase mismatch amongst the various degrees-of-freedom as already discussed. Using existing power conditioning circuitry, at least six sets of circuits would be required in order to effectively extract the electrical energy, which was impractical within the scope of this study.

4.3. Results

In addition to the circular membrane 01 mode at around 1.4kHz, the first transverse modes of the five subsidiary cantilevers within the new structure can also be employed (~ 280 Hz to ~ 320 Hz) to open up additional operational frequency bands. In contrast, the classic membrane only has an active response when the 01 mode is triggered at 1.2kHz. Figure 13 illustrates the frequency domain characteristics of the device. Driven at 0.5g input acceleration, the plain membrane recorded $\sim 0.42 \mu\text{W}$ average power at the 01 mode while the new topology device yielded $\sim 0.66 \mu\text{W}$ at the comparable resonant peak.

Due to practical restraints, the power output of the new topology was 'diluted' by sharing the electrode connection with the cantilevers, which were minimally responsive at the 01 mode frequency range. However, the high strain

regions recovered from the membrane core still placed the new design favourably against its classical counterpart. Furthermore, the subsidiary cantilevers had a much higher compliance than the membrane and produced up to $0.25 \mu\text{W}$ (each) prior to fracture when driven beyond 0.5g of acceleration at resonance.

Even prior to operation, the new design exhibited relatively lower yield, as the subsidiary cantilevers were more prone to fracture during fabrication and handling. On the other hand, the classical membrane was more robust and did not exhibit failure within the scanned range of acceleration.

The Broadband responsiveness of the devices were investigated by introducing band-limited white noise from 10 Hz to 2kHz. Figure 14 is an example of the time domain voltage response from the devices. It can be seen that the cantilevers-on-membrane device yielded about 1.6 times higher RMS voltage in this instance.

Figure 15 compares the average power output of the new membrane structure with the classic membrane structure when subjected to band-limited white noise from 10 Hz to 2kHz. The experimentally matched load resistance ranged between 50 k Ω to 100 k Ω . However, these values represent a compromise due to the impedance mismatch of the piezoelectric regions on the membrane and the cantilevers.

Up to approximately twofold power enhancement was observed between 0.005 g² Hz⁻¹ and 0.02 g² Hz⁻¹ of band-limited white noise. While subsidiary cantilevers readily fractured when driven beyond 0.5g at resonance, such mechanical failures were not observed when subjected towards the band-limited white noise excitation of up to 0.05 g² Hz⁻¹ with peaks at 10g. Therefore, this demonstrates the suitability of this approach when applied to broadband noise excitations.

5. Conclusion

A new cantilevers-on-membrane topology for MEMS piezoelectric vibration energy harvesting is proposed. Instead of positioning the proof mass at the centre of a classic plain membrane, the masses are distributed onto subsidiary cantilevers. This enabled the harvesting of strain energy at the centre core of the membrane, which would otherwise be neutralised. Furthermore, additional frequency bands were introduced from the subsidiary cantilevers, thus making it more responsive to broadband excitation. Simulation results suggest the theoretical potential to recover about an order of a magnitude higher power for a given acceleration loading, under ideal conditions. Experimentally, the new membrane harvester recorded a power output up to two times higher than a plain membrane when subjected to band-limited white noise vibration.

Acknowledgment

This work was supported by the Engineering and Physical Sciences Research Council (EPSRC grant number: EP/L010917/1).

References

- [1] Harb A 2011 Energy harvesting: state-of-the-art *Renew. Energy* **36** 2641–54
- [2] Beeby S P, Tudor M J and White N M 2006 Energy harvesting vibration sources for microsystems applications *Meas. Sci. Technol.* **17** R175–95
- [3] Priya S and Inman D J 2009 *Energy Harvesting Technologies* (New York: Springer)
- [4] Peano F and Tambosso T 2005 Design and optimization of a mems electret-based capacitive energy scavenger *J. Microelectromech. Syst.* **14** 429–35
- [5] Suzuki Y, Miki D, Edamoto M and Honzumi M 2010 A mems electret generator with electrostatic levitation for vibration-driven energy harvesting applications *J. Micromech. Microeng.* **20** 104002
- [6] Wang Z L 2014 Triboelectric nanogenerators as new energy technology and self-powered sensors—principles, problems and perspectives *Faraday Discuss.* **174** 447–58
- [7] van Schaijk R, Elfrink R, Kamel T and Goedbloed M 2008 Piezoelectric aln energy harvesters for wireless autonomous transducer solutions *IEEE Sensors (Lecce, 26–29 October 2008)* pp 45–8
- [8] Andosca R, Gus McDonald T, Genova V, Rosenberg S, Keating J, Benedixen C and Wu J 2012 Experimental and theoretical studies on mems piezoelectric vibrational energy harvesters with mass loading *Sensors Actuators A* **178** 76–87
- [9] Yoo S, Kim J, Park S, Jang C and Jeong H 2014 Membrane-type vibrational energy harvester based on a multi-layered piezoelectric membrane *J. Korean Phys. Soc.* **64** 706–9
- [10] Besse N, Quintero A V, Briand D, Janphuang P, Lockhart R, Ruan J J and de Rooij N F 2012 Pzt-based energy harvesters on plastic foil optimized through theoretical modeling and fabrication improvements *PowerMEMS (Atlanta, GA, USA, 2–5 December 2012)* pp 42–5
- [11] Aktakka E E, Peterson R L and Najafi K 2011 Thinned-pzt on SOI process and design optimization for piezoelectric inertial energy harvesting *Transducers (Beijing, China, 5–9 June 2011)* pp 1649–52
- [12] Tsujiura Y, Suwa E, Hida H, Suenaga K, Shibata K and Kanno I 2013 Lead-free piezoelectric mems energy harvesters of stainless steel cantilevers *Transducers (Barcelona, Spain, 16–20 June 2013)* pp 474–7
- [13] Minh L V, Hara M and Kuwano H 2012 Miniaturised multi-beam (k,na)nbo3-based energy harvester *PowerMEMS (Atlanta, GA, USA, 2–5 December 2012)* pp 34–7
- [14] Jia Y and Seshia A A 2015 Power optimization by mass tuning for MEMS piezoelectric cantilever vibration energy harvesting *J. Microelectromech. Syst.* **25** 108–17
- [15] Jia Y and Seshia A A 2014 Comparison of five topologies of cantilever-based mems piezoelectric vibration energy harvesters *J. Phys.: Conf. Ser.* **557** 012086
- [16] Jia Y and Seshia A A 2015 Five topologies of cantilever-based mems piezoelectric vibration energy harvesters: a numerical and experimental comparison *Microsyst. Technol.* **1**–12
- [17] MicroGen 2013 Bolt r0600 datasheet *Technical Report* MicroGen Systems
- [18] Zhu D, Tudor M J and Beeby S P 2010 Strategies for increasing the operating frequency range of vibration energy harvesters—a review *Meas. Sci. Technol.* **21** 022001
- [19] Jia Yu, Du S and Seshia A A 2015 Cantilevers-on-membrane design for broadband mems piezoelectric vibration energy harvesting *J. Phys.: Conf. Ser.* **660** 012030
- [20] Kong N, Ha D S, Erturk A and Inman D J 2010 Resistive impedance matching circuit for piezoelectric energy harvesting *J. Intell. Mater. Syst. Struct.* **21** 1293–302
- [21] Schomburg W K 2011 Chapter Membranes *Introduction to Microsystem Design* (Berlin: Springer) pp 29–52
- [22] Piersol A G and Paez T L 2009 *Shock and Vibrations Handbook* 6 edn (New York: McGraw-Hill)